A novel theranostic strategy for MMP-14 expressing glioblastomas impacts survival

Suchismita Mohanty[1], Zixin Chen[1], Kai Li[1], Goreti Ribeiro Morais[2], Jessica Klockow[1], Ketan Yerneni[3], Laura Pisani[1], Frederick T Chin[1], Siddharta Mitra[4], Samuel Cheshier[4], Edwin Chang, Sanjiv Sam Gambhir[1,5,6], Jianghong Rao[1], Paul M. Loadman[2], Robert A. Falconer[2], Heike E Daldrup-Link[1*],

[1] Department of Radiology, Molecular Imaging Program at Stanford (MIPS), Stanford University

[2] Institute of Cancer Therapeutics, Faculty of Life Sciences, University of Bradford, Bradford, UK

[3] Department of Biology, Skidmore College

[4] Department of Neurosurgery, Institute for Stem Cell Biology and Regenerative Medicine and Division of Pediatric Neurosurgery, Lucile Packard Children's Hospital, Stanford University, Stanford, CA USA.

[5] Department of Bioengineering, Stanford University,

[6] Department of Materials Science & Engineering, Stanford University

Running Title: Clinically translatable therapy for human glioblastomas

Keywords: Glioblastoma, glioblastoma initiating cells, imaging, therapy and theranostic nanoparticle.

Abbreviations: Glioblastoma (GBM), glioblastoma initiating cell (GIC), cross-linked iron oxide nanoparticle (CLIO), matrix-metalloproteinase (MMP), vasculature disrupting agent (VDA), enhanced permeability and retention (EPR), temozolomide (TMZ), magnetic resonance imaging (MRI), bioluminescence imaging (BLI), azademethylcolchicine-peptide conjugate (ICT2588), modified analogue of ICT2588 (ICT)

Financial support: Heike E Daldrup-Link, NIH, R21CA176519 and R21CA190196; Sanjiv Sam Gambhir, NIH, 1U54CA199075; Jessica Klockow, NCI training grant, T32CA118681, Robert A. Falconer, University of Bradford, UoB-66031

*__Corresponding author__:

Heike E Daldrup-Link M.D. PhD

725 Welch Rd, Rm 1665

Stanford, CA 94305-5614

Ph: (650) 723-8996

Fax: (650) 725-8957

H.E.Daldrup-Link@stanford.edu

Abstract

Glioblastoma (GBM) has a dismal prognosis. Evidence from preclinical tumor models and human trials indicates the role of GBM initiating cells (GIC) in GBM drug resistance. Here, we propose a new treatment option with tumor enzyme-activatable, combined therapeutic and diagnostic (theranostic) nanoparticles, which caused specific toxicity against GBM tumor cells and GICs. The theranostic cross-linked iron oxide nanoparticles (CLIO) were conjugated to a highly potent vascular disrupting agent (ICT) and secured with a matrix-metalloproteinase (MMP-14) cleavable peptide. Treatment with CLIO-ICT disrupted tumor vasculature of MMP-14 expressing GBM, induced GIC apoptosis and significantly impaired tumor growth. In addition, the iron core of CLIO-ICT enabled *in vivo* drug tracking with MR imaging. Treatment with CLIO-ICT plus temozolomide achieved tumor remission and significantly increased survival of human GBM bearing mice by more than 2 fold compared to treatment with temozolomide alone. Thus, we present a novel therapeutic strategy with significant impact on survival and great potential for clinical translation.

Introduction

Glioblastoma multiforme (GBM) is the most frequent primary malignant brain tumor in adults and the leading cause of cancer-related death in children (1). The mean survival time is 12 months in both adults and children (2). GBM contains GBM-initiating cells (GICs) that play a central role in GBM development and disease recurrence (3). GICs possess enhanced self-renewal and invasive properties, promote tumor angiogenesis and are resistant to the limited number of current therapies, notably temozolomide (4,5). Therefore, GICs represent the core problem of the dismal outcome of GBM. To achieve improved survival of GBM patients, novel therapeutic strategies are needed that target GICs.

GICs are preferentially found in the perivascular niche (6,7) and depend on tumor vessels for nutrition supply and survival (8). The efficacy of current GBM therapies with oral or intravenous drugs is hindered by their limited trans-endothelial permeability to the GIC niche. Previous drug-loaded nanocarrier systems relied on the enhanced permeability and retention (EPR) effect in tumors (9,10). However, the highly heterogeneous nature of the EPR effect can lead to poor delivery to the GIC niche and hence, poor therapeutic efficacy (10). A new, emerging strategy is to deliver vascular-disrupting agents (VDAs), which do not rely on the EPR effect. VDAs target endothelial cells at the intraluminal surface of blood vessels, for example, by disrupting the colchicine-binding site of tubulin (11,12). This leads to vascular collapse and starvation

of tumor cells supplied by these vessels, a very effective therapeutic strategy (12,13). In addition, VDAs selectively destabilize the tumor microvascular endothelial lining, causing a transient increase in vascular permeability and drug delivery to the perivascular tumor interstitium (14,15), the location of the GIC niche. Thus, the highly vascularized nature of GBMs and perivascular location of the GIC-vascular niche have spurred a lot of interest in VDAs. Previous VDAs, including combretastatin and 5,6-dimethylxanthenone-4-acetic acid, have led to significant necrosis in gliomas (16,17). However, the clinical efficacy of first generation VDAs was limited by a high prevalence of cardiotoxicity (18-20).

To avoid concomitant toxic effects in normal organs, nontoxic VDA-prodrugs can be designed, which are activated by specific tumor enzymes (21). For example, matrix metalloproteinases (MMPs) and specifically the membrane-type MMPs (MT-MMPs; MT1-MMP = MMP-14) subclass represent a ideal target for prodrug activation, because they are highly overexpressed in GBM (22-24) and can selectively cleave specific peptide sequences (21,25-27). The azademethylcolchicine-peptide conjugate ICT2588 is metabolized by MMP-14 to release an active VDA, azademethylcolchicine, with efficacy against a range of solid tumors (26) and minimal systemic toxicity (28). We coupled ICT, a minor structural analogue of ICT2588 (modified to allow conjugation to nanoparticles), to cross-linked iron oxide nanoparticles (CLIO) to generate theranostic nanoparticles (CLIO-ICT). Initial feasibility studies showed MMP-14-specific cleavage, efficient drug delivery and therapeutic efficacy in murine mammary adenocarcinomas (29). This new theranostic strategy should be particularly beneficial for GBM, where

efficient drug treatment is limited by the blood-brain-barrier and inability to reach the perivascular GIC niche. Based on the vascular disrupting properties of the ICT drug (26), CLIO-ICT should be able to permeate the tumor microvascular endothelium and reach tumor cells and GICs. Thus, we hypothesized that CLIO-ICT will induce significant apoptosis of GBM tumor cells and GIC, and thereby, prolong survival of GBM bearing mice.

Materials and Methods

Chemicals and Antibodies

The following antibodies were used: α-tubulin (Abcam), CD133 (Miltenyi Biotech), CD49F (Biolegend), CD15 (BD Biosciences), CD31 (Abcam), MMP-14 (Abcam), Nestin (Abcam) and cleaved caspase-3 (Cell Signaling Technology). The following chemicals were used: Ferumoxytol (AMAG Pharmaceuticals), Temozolomide (Sigma), Ilomastat (Selleckchem).

Synthesis and characterization of CLIO-ICTs

ICT and CLIO-ICT were synthesized according to a previously published protocol (29). To determine the relaxivities of ferumoxytol and CLIO-ICT, *in vitro* MRI studies were conducted on a 7T MR scanner (Bruker Biospin, Billerica, MA). The transverse relaxation times (T_2) of ferumoxytol and CLIO-ICT in water with various of Fe concentrations (0, 2.5, 5, 10, 20, 40 μg/mL) were measured individually using a fast spin echo sequence with a repetition time (TR) of ~ 3000 ms, multiple echo times (TE) of 6.8,

13.6, 20.4, 27.3, 34 and 40.9 ms. The T_2 relaxivity values (r_2) was obtained from linear least-squares determination of the slope of $1/T_2$ relaxation rate (s^{-1}) versus the Fe concentration plot. The concentration of iron (Fe) was determined using inductively coupled plasma-mass spectrometry (ICP-MS) and the iron (Fe) atoms in each iron oxide core was estimated to be ~6200 using Diamond® crystal structure analysis software. The molar concentration of iron (Fe) in CLIO-ICT stock solution was then calculated. Since ICT is linked with FITC, the average amount of ICT covalently immobilized to a single CLIO-ICT nanoparticle was determined by the emission intensity of FITC. In brief, the emission profile of FITC of a diluted CLIO-ICT solution was recorded upon excitation at 495 nm. The concentration of FITC was then estimated using a calibration plot obtained from a set of standard FITC solutions. The average number of ICT on each CLIO-ICT was then obtained. To determine the sizes of ferumoxytol and CLIO-ICT, the samples in DI water at a Fe concentration of 100 μg/mL were analyzed using a Zetasizer Nano ZS equipment.

Cell Culture

Two patient-derived GBM cell lines (pcGBM2, pcGBM39) and three commercially available GBM cell lines (U87-MG, U138 and A172 from ATCC, Manassas, VA, USA) were used for *in vitro* studies. Both pcGBM2 and pcGBM39 were kindly provided by Dr. Sanjiv Sam Gambhir, Stanford University. HCN2, normal cortical neuron cells were purchased from ATCC. U87-MG, U138, A172 cells were grown in DMEM (Life Technologies) containing 10% FBS and 1% Penicillin/Streptomycin (Life Technologies). HCN2 cells were grown in DMEM with 4 mM L-glutamine adjusted to contain 1.5 g/L

sodium bicarbonate, 4.5 g/L glucose, 90%; fetal bovine serum, 10%. pcGBM2 and pcGBM39 were cultured as floating cellular spheres as previously described (30). All cell lines used were authentic and confirmed to be mycoplasma negative using the MycoAlert Mycoplasma Activity Kit (Lonza). To test for mycoplasma activity, MycoAlert substrate was added to the test media (cell supernatant) which catalyzes the conversion of ADP to ATP by mycoplasma enzymes in the cell supernatant. This was followed by addition of a luciferase reaction mix that cleaved ATP to produce a bioluminescent signal as an indication of mycoplasma activity. All cell lines used were from early passages.

Assessment of MMP-14 gene expression of different patient-derived GBM neurospheres (pcGBM2 and pcGBM39) and GBM cell lines (U87-MG, U138 and A172) as well as human neuronal cortical cells (HCN2) as controls was determined by qPCR as previously described (29). qPCR expression analysis for MMP-14 and the control marker GAPDH was done and the total cellular RNA was extracted from each sample with the QIAGEN RNeasy® mini kit. cDNA was prepared from total RNA and quantitative real-time PCRs (qPCRs) were carried out and analyzed on an Applied Biosystems StepOne™ Real-Time PCR System. The formation of double-stranded DNA product was monitored by TaqMan® gene expression primers.

In vitro evaluation of the therapeutic efficacy of CLIO ICT against GBM cancer cells and GIC

Patient-derived GBM neurospheres (pcGBM2 and pcGBM39) and GBM cell lines (U87-MG, U138 and A172) as well as human neuronal cortical cells (HCN2) cells were plated

in 96 well plates at 2×10^4 cells/well and treated with CLIO-ICT (10 nM), ICT (10 nM), CLIO (0.01 mM) and DMSO at 37°C, 5% CO_2.

Cell viability after 96 hours was assessed using MTS assay kit (Promega) as per the manufacturer's instruction. At the end of the incubation period, the absorbance was measured at 490 nm in a microplate reader (Expert Plus V1.4 ASYS). Cell viability was also verified with cell counting following addition of trypan blue (Sigma) at a final concentration of 0.1% (v/v), and routine examination of the cells under phase contrast microscopy.

For apoptotic assays control and treated pcGBM2, pcGBM39 U87-MG, U138 and A172 and HCN2 cells were analyzed for caspase-3 activity levels, a marker of cytotoxicity using the SensoLyte ® Homogeneous AMC Caspase-3/7 assay kit (AnaSpec, Inc., California), according to the manufacturer's instructions. Release of the AMC fluorophore following cleavage of the specific fluorometric caspase substrate, DEVD-AMC was detected using a fluorometer (ex/em = 354 nm/442 nm). Data were normalized relative to the vehicle-treated controls. For flow cytometry-based apoptosis detection, control and CLIO-ICT-treated pcGBM39, U87-MG and A172 cells were also analyzed by Annexin V-based methods using Annexin V Apoptosis Detection Kit (eBioscience, Inc., San Diego, CA). Additionally, control and CLIO-ICT pcGBM39 cells were scored for anti-active Caspase-3 (BD Biosciences, San Jose, CA) with flowcytometry (BD FACS ARIA II, BD).

For characterization of GICs, pcGBM39 and pcGBM2 were stained for cancer stem cell markers using anti-CD133-Biotin (Miltenyi Biotech), CD15-FITC (BD Biosciences) and CD49F-PE-Texas red (Biolegend) and analyzed with flow cytometry Immunofluorescence staining for α-tubulin (Cell Signaling Technology) at 1:25 dilution was conducted as previously described.

In vivo evaluation of the therapeutic efficacy of CLIO ICT against GBM cancer cells and GIC

In vivo intracranial xenografts

300,000 cells were injected stereotaxically into the striatum of anesthetized 6 to 8 week old NOD scid gamma (NSG) mice, using the following coordinates: 2 mm posterior to the bregma, 2 mm lateral to the midline, and 3–4 mm deep with respect to the surface of the skull. Once tumor masses were detected with bioluminescence imaging, mice were randomized in four groups and CLIO-ICT, ICT, CLIO or PBS were delivered intravenously twice a week for 14 days. Total cumulative doses for each drug regimen were: CLIO-ICT (80mg/kg of ICT), ICT (80mg/kg of ICT) and CLIO (0.5 mmol Fe/kg). For combination treatment with temozolomide (33mg/kg), mice were treated with ICT and CLIO-ICT twice a week for 21 days. Total cumulative doses for TMZ were 200 mg/kg respectively. For determining in vivo tumorigenesis of GICs, 500 $CD133^{+}CD15^{+}$, $CD133^{-}CD15^{-}$, $CD49F^{+}CD15^{+}$, $CD49F^{+}CD15^{-}$ pcGBM39 cells were injected stereotaxically into the striatum of anesthetized 6 to 8 week old NOD scid gamma (NSG) mice as described above. Animals were scored for tumor formation with

bioluminescence assays until 4 months. All animal maintenance, handling, surveillance, and experimentation were performed in accordance with and approval from the Stanford University Administrative Panel on Laboratory Animal Care (Protocol 24965).

Bioluminescent imaging

Luminescent imaging was performed 30 days (for pcGBM39) and 60 days (for pcGBM2) after tumor injection on an IVIS Spectrum (Caliper Life Science) and quantified using Living Image 4.0 software. D-luciferin (firefly) potassium salt solution (Biosynth) was prepared (15 mg/ml) and injected intraperitoneally (0.139 g luciferin per kg body weight). Total flux (photons per second) values were obtained by imaging mice until peak radiance was achieved and quantified with Living Image 4.0 software. Bioluminescent imaging was repeated at the end of the treatment and analyzed in a blind manner.

Immunocytochemistry

Mice were euthanized at the end of the treatment for further histological examination. For histological analysis, the brains were kept in 10% neutral buffered formalin for 24 h, followed by 70% ethanol at room temperature for 24 h. Brains were then embedded in paraffin for 3 h at 67°C. Coronal sections (5 μm thick) were stained with hematoxylin and eosin, and images were acquired (Eclipse E800, Nikon, USA). Brain tissues were also fixed in 4% paraformaldehyde at 4°C overnight and later immersed in 30% sucrose for 2 days. Brains were then embedded in OCT and stored in -80°C. Coronal sections (5 μm thick) were mounted on superfrost slides, rinsed with phosphate buffered saline

(PBS) and permeabilized with 0.1% Triton X-100 made in PBS solution for 15 min. Subsequently cells were blocked for 2 hours and stained with primary antibodies overnight to determine GIC populations or to evaluate apoptosis upon treatment with theranostic nanoparticles. The following dilutions were used: MMP-14 (1:200, Abcam), Nestin (1:200, Abcam), cleaved Caspase-3 (1:300, Cell Signaling Technology), CD133 (1:10, Miltenyi Biotec), and CD15 (1:200, Abcam). Immunofluorescence images were acquired with a Leica SP8 confocal microscope using Leica AF software. Images were prepared using Adobe Photoshop (Adobe Systems) and analyzed using Velocity 64 software.

Microvessel density

Coronal sections (5 µm thick) from PBS, CLIO, ICT and CLIO-ICT treated animals were mounted on superfrost slides, rinsed with phosphate buffered saline (PBS), and permeabilized with 0.1% Triton X-100 made in PBS solution for 15 min. Subsequently cells were blocked for 2 hours and stained with CD31 (1:20, Abcam) antibody overnight to determine endothelial cells. Nuclei were counterstained with DAPI and imaged in Leica SP5 confocal microscope. Single endothelial cells or clusters of endothelial cells positive for CD-31 were considered as a vessel. At first, slides were examined at an original magnification of 10×. Three “hot spots“ (areas with the highest microvessel concentration) from each slide were identified and these areas were photographed at 10x. The area of this field was recorded and the number of microvessels in this field will be counted with Image-J in a blindfolded manner. MVD (microvessel/mm^2) were then

assessed according to Weidner *et al*.,(31). MVD of the specimen were estimated as a mean ± SD of MVD in three different fields from three independent experiments.

Flow cytometry

For detection of apoptosis in GICs and GBM cancer cells, mice were euthanized, and brain tumors were dissociated to single cells and stained with anti-CD15-APC (BD Biosciences) or Annexin V-PE (BioLegend) and DAPI. Tumor cells were gated based on GFP expression and mouse cells were gated out using a lineage mixture of Brilliant Violet 605-conjugated $H2k^b$, $H2k^d$ Ter119, and CD45 antibodies. Flow cytometric analysis and cell sorting were performed on a BD FACS ARIA II (BD) flowcytometer.

MRI

We evaluated tumor delivery of CLIO-ICT in GBM-bearing mice using MRI. CLIO-ICT comprised of ferumoxytol (CLIO-M) linked to ICT. Ferumoxytol (AMAG Pharmaceuticals) comprised of iron oxide nanoparticles that had a mean hydrodynamic diameter of 30 nm and provided superparamagnetic signal effects on T_1- and T_2-weighted MR images. pcGBM39-bearing mice underwent MRI before and 24 hours after intravenous injection of PBS, CLIO, ICT and CLIO-ICT (n=6) and at regular intervals during treatments. MRI studies of GBM-bearing mice were performed on a 7T MR scanner (Bruker Biospin, Billerica, MA), using a field of view of 2 cm × 2 cm and a slice thickness of 0.5mm for the following acquisitions: T_2-weighted fast spin echo (FSE): repetition time (TR): 4500 ms, echo time (TE): 42 ms, flip angle α: 90° and T_2 multi-slice

multi-echo (MSME): TR: 3000 ms, TE: 8, 16, 24, 32, 40, 48, 56, 64, 72, 80, 88 and 96 ms, α: 90°. T_2 relaxation times of the tumors were calculated as a quantitative measure of tumor contrast enhancement.

Histopathologic correlations of MRI data.

For Prussian blue iron stains, coronal brain tissue sections (5 μm) of formalin-fixed, paraffin-embedded tissue were deparaffinized with xylene, rehydrated, and stained according to the manufacturer's recommendation with the Sigma-Aldrich Accustain Iron Stain Kit. Sections were counterstained with nuclear fast red (Fisher Scientific). Representative images were captured using the Aperio ScanScope CS Slide Scanner with a 20x objective for whole-slide imaging.

Inductively Coupled Plasma Mass Spectrometry (ICP-MS)

ICP-MS analysis was conducted to study the biodistribution of theranostic CLIO-ICT nanoparticles. Briefly, 6-to 8-week-old NOD scid gamma (NSG) mice (n=3) were intravenously injected with PBS and CLIO-ICT (80mg/kg of ICT, 0.5 mmol Fe/kg). After 24 hours, mice were euthanized and different organs including brain, heart, lung, liver, kidney and spleen were harvested and processed for ICP-MS (Inductively Coupled Plasma Mass Spectrometry) analysis. The tissues were weighed in pre-weighed glass tubes and treated with concentrated HNO_3 (1g tissue/ml HNO3) and 50 μl H_2O_2. The tubes were immersed in oil bath at 110^{o}C overnight to completely digest the samples. Samples were considered completely digested when there was no liquid left in tubes. The samples were diluted with 5mL of 2% HNO_3, gently vortexed and filtered through

0.44micron Millipore filter and subjected to ICP-MS analysis. A standard solution of iron in the detection range was also included. Amount of iron per sample was obtained and expressed as iron per gram of tissue.

Determination of plasma vWF

We also evaluated the levels of von Willeband Factor (vWF) in plasma from animals treated with PBS, ICT and CLIO-ICT. vWF is a marker of cardiotoxicity and was detected with kit based ELISA assays (MyBiosource.com) following manufacturer's protocol. Briefly, blood was collected from animals on day 5 after treatment with PBS, ICT and CLIO-ICT into heparinized tubes to separate the plasma and stored in -80°C. The plasma was diluted 1:3 and 100 μl of samples or standards were added to murine vWF antibody pre-coated plates for 90 min at 37°C. The plate was washed with washing solution from the kit, followed by incubation with biotinylated vWF antibody for 60 min at 37°C. Then the plate was washed again and enzyme-working solution was added for 30 min at 37°C. After five washes 100 μl of color reagent was added for not more than 30 min. The reaction was then stopped and OD values were measured at 450nm on a microplate reader. A known concentration of vWF was used to generate a standard curve. The OD of samples was plotted over a standard curve and the concentration of plasma vWF was calculated after accounting for dilution factor. Our results indicated that CLIO-ICT and ICT did not induce any further increase in plasma vWF levels as compared to PBS. However mice administered with doxorubicin showed slightly higher levels of vWF and served as our positive control.

Statistical analysis

Cell viability and apoptosis experiments were performed in biological triplicates, in three independent experiments. Magnetic resonance, Immunofluorescence, and flow cytometry images were representative from three independent experiments. Results were presented as mean ± SD unless otherwise presented. Tumor and organ relaxation rates and fluorescence signals were compared within multiple experimental groups using one-way ANOVA. Results were analyzed using nonparametric two-tailed Mann–Whitney test to compare two groups. Kaplan–Meier survival curves were compared using the log-rank (Mantel–Cox) test. The level of significance was set at $p < 0.05$, as compared with the control group. Statistical analyses were carried out with Prism 6.0 software (GraphPad).

Results

Physicochemical properties of CLIO-ICTs

The concept for MMP-14 activatable theranostic nanoparticles, CLIO-ICTs in GBMs is shown in Fig. 1a. ICT and CLIO-ICT were prepared and characterized as previously described (29). The hydrodynamic diameter of CLIO-ICT nanoparticles, as measured with a Zetasizer Nano ZS analyzer, was 22.10 ± 0.78 nm, slightly larger than ferumoxytol nanoparticles (20.27± 1.02 nm). The average number of ICT molecules per iron oxide nanoparticle was 4.7, based on the attached fluorescein absorption and known CLIO-ICT concentration. CLIO-ICTs had higher r_2 relaxation rates (276.07 mM^{-1}

s^{-1}) compared to original ferumoxytol nanoparticles (101.18 mM^{-1} s^{-1}, respectively) (Fig. 1b). This is likely due to the modified surface coating.

In-vitro anti-tumor effects of CLIO-ICTs in human GBMs

To evaluate MMP-14 levels, we analyzed the gene expression profile of MMP-14 by qPCR in five human GBM cell lines. HCN2, a cell line derived from normal neural cortex expressed very low levels of MMP-14 and served as our negative control (Fig. 1c). Expression data for MMP-14 was collected as Ct values and the gene expression levels were normalized to the reference control gene, GAPDH. While the cell lines U87 and U138 expressed increased levels of MMP-14 compared to HCN2 cells ($p < 0.005$), the A172 cell line showed no significant MMP-14 expression ($p = 0.103$; Fig. 1c). Neurospheres were derived from two GBM patients and cultured in neurosphere medium (30,32). Compared to HCN2 cells, both pcGBM2 ($p = 0.0027$; Fig. 1c) and pcGBM39 ($p = 0.001$; Fig. 1c) showed significantly increased MMP-14 expression.

Next, we investigated the effect of theranostic CLIO-ICT nanoparticles on GBM cell viability. In all MMP-14 high GBM cell lines, treatment with both ICT (10 nM) and CLIO-ICT (10 nM ICT; 0.01 mM CLIO) induced significant ($p < 0.005$) loss of cell viability when compared to CLIO (0.01 mM) or DMSO (Fig. 1d). A172 cells were not responsive to treatment and MMP-14 negative normal neural cortex cells (HCN-2) did not show any significant cytotoxic effects after incubation with CLIO-ICT or ICT (Fig. 1d). The dose range of CLIO-ICT and ICT was chosen based on previous studies (29,33,34) and in the case of CLIO, was calculated on the basis of plasma concentrations of CLIO reached in patients after clinically applied doses (35-37). In apoptosis assays, GBM

cells expressing high MMP-14 showed higher signal for both active caspase-3 fluorescence and Annexin-V/PI staining after incubation with CLIO-ICT and ICT (Fig. 1e, 1f and Supplementary Fig. 1a). A172 and HCN2 cells demonstrated minimal induction of caspase-3 upon treatment with CLIO-ICT (Fig. 1e). Additionally experiments with MMP inhibitor Ilomastat rescued CLIO-ICT toxicity in GBMs, suggesting that activation of the CLIO-ICT was MMP-specific (Supplementary Fig. 1b). These results are consistent with MMP-14 selectivity shown for CLIO-ICT and ICT2588 as shown in previous studies (26,29).

The apoptotic effects of most VDAs are a result of tubulin disruption in tumor cells and tumor endothelial cells. To evaluate if our theranostic nanoparticles retained this therapeutic effect, we conducted α-tubulin staining in treated and control MMP-14 expressing GBM cells. Cells treated with both CLIO-ICT and ICT showed dramatic alteration in tubulin morphology (Fig. 1g). Control cells showed normal tubulin morphology as depicted by spindle shape of the microtubule structures whereas treated cells showed retracted tubulin fibers that were aggregated around the nuclear periphery. The amount of tubulin was significantly reduced in presence of CLIO-ICT, which was quantified as total fluorescence in the red channel. Colchicine-treated cells were used as positive controls in these experiments (Supplementary Fig. 1c).

CLIO-ICTs induce apoptosis in GBM initiating cells (GICs) *in vitro.*

To study the therapeutic effects of CLIO-ICTs on GICs, we incubated GBM cultures with CLIO-ICT (10 nM) and examined GIC apoptosis by Annexin-V/DAPI staining.

We defined GICs (Supplementary Fig. 2) by a combination of established cell surface

markers, CD133, CD15 and CD49F (38,39). Considering the heterogeneity of tumors, we confirmed the reliability of these markers in identifying GICs in pcGBM39 and pcGBM2 (Supplementary Fig. 2), sorting $CD133^{+}CD15^{+}$, $CD133^{-}CD15^{-}$, $CD49F^{+}CD15^{+}$ and $CD49F^{+}CD15^{-}$ cells from pcGBM39 and conducting *in vivo* tumorigenic assay (Supplementary Fig. 3). When injected into the right parietal lobe of NSG mice, only the $CD15^{+}/CD133^{+}$ and $CD49F^{+}/CD15^{+}$ population would generate tumors as early as 8 weeks, suggesting their tumorigenic potential. This confirmed the GIC like phenotype of these cells (Supplementary Fig. 3a, b).

Next, we investigated whether CLIO-ICTs could induce apoptosis of GICs. pcGBM39 cells treated with CLIO-ICT demonstrated a significant reduction in the percentage of $CD133^{+}$, $CD15^{+}$ and $CD49F^{+}$ populations ($p < 0.05$; Fig. 1h, 1i). Further, $CD133^{+}$, $CD15^{+}$ and $CD49F^{+}$ cells from CLIO-ICT-treated pcGBM39 showed significant apoptosis as detected by Annexin-V/DAPI staining ($p < 0.005$; Fig. 1h, 1i).

Anti-tumor effects of CLIO-ICTs in orthotopic brain tumors initiated from patient-derived GBM neurospheres.

Since the VDA activity in tumors is documented (26), we hypothesized that CLIO-ICT will target tumor vasculature, GICs and GBM cancer cells (Fig. 2a). To establish an orthotopic mouse model for GBM, tumor cells from patient-derived GBM neurospheres, pcGBM2 and pcGBM39 were injected into right parietal lobes of NSG mice and tested for efficacy of CLIO-ICT (Fig. 2b). The *in vivo* growth of these GBM neurospheres has been previously documented (30,32). MMP-14 expression in these tumors was confirmed prior to drug treatment (Supplementary Fig. 4). Both pcGBM2 and pcGBM39

were engineered to express firefly-luciferase-GFP and firefly-luciferase expressing reporter respectively for *in vivo* tumor detection with *in vivo* bioluminescence imaging.

At 3 to 4 weeks post-intracranial cell injection, pcGBM39 tumors were detectable in the brain whereas pcGBM2 tumors took longer (8 weeks). Mice were randomized into four treatment cohorts: each were i.v injected with CLIO-ICT, ICT, CLIO or PBS twice a week for 14 days. Total cumulative doses for each drug regimen were: CLIO-ICT (80mg/kg of ICT), ICT (80mg/kg of ICT) and CLIO (0.5 mmol Fe/kg). A longitudinal time course study was performed to study the anti-tumor properties of the theranostic nanoparticles. Both CLIO-ICT and ICT had significant anti-tumor effects on two different GBM types, whereas PBS-treated animals demonstrated increase in tumor size (Fig. 2c). No tumor response was observed in the CLIO-treated mice, suggesting that the therapeutic effect is derived directly from the released VDA entity (Fig. 2c). CLIO-ICT significantly inhibited pcGBM39 tumor growth and achieved remission of pcGBM2 tumors (Fig. 2c, 2d, $p < 0.005$). PBS or CLIO-treated animals drastically lost body weight over time, while CLIO-ICT and ICT-treated sets demonstrated no significant weight loss ($p > 0.05$; Supplementary Fig. 5). CLIO-ICT improved survival by 100%, 200% and 220% compared to ICT, CLIO or PBS-treated mice ($p < 0.05$; Fig. 2e). Pathologic evaluation confirmed decreased tumor size and increased tumor apoptosis following CLIO-ICT treatment compared to CLIO or PBS-treatment (Fig. 3a, 3b). We also investigated the biodistribution of CLIO-ICT in tumor free NSG mice using Inductively Coupled Plasma Mass Spectrophotometry (ICP-MS). Results show that CLIO-ICT was accumulated in lungs, liver, spleen and kidney (Supplementary Fig. 6a, p

< 0.05). Brain and heart showed very little CLIO-ICT (Supplementary Fig. 6a, $p > 0.05$). Next we measured CLIO-ICT toxicity in normal organs (brain, heart, lung, liver, spleen and kidney) by evaluating the amount of apoptotic marker, caspase-3. Immunofluorescence data showed negligible expression of active caspase-3 in these organs from CLIO-ICT-treated animals when compared to PBS-treated group (Supplementary Fig. 6b). Since previous VDAs are known to induce cardiotoxicity, we further confirmed that CLIO-ICT is minimally cardiotoxic. In addition to caspase-3 staining, we also measured plasma vWF levels in both PBS and CLIO-ICT-treated animals. vWF is conventionally used as a marker for cardiotoxicity (28). Our data show that no significant difference was observed for plasma vWF levels in PBS and CLIO-ICT treated animals. In summary CLIO-ICT was found to be non-toxic to normal organs (Supplementary Fig. 6c).

To further compare tumor retention of macromolecular CLIO-ICT and small molecular ICT, we measured drug quantities of FITC-labeled ICT and CLIO-ICT in pcGBM39 tumor specimen with immunofluorescence assays. CLIO-ICT treated tumors demonstrated significantly higher FITC intensity as compared to ICT only ($p < 0.05$), suggesting improved tumor retention of ICT when linked to a nanocarrier (Fig. 3b).

To better understand the tumor retention of CLIO-ICT *in vivo*, we next imaged pcGBM39-bearing mice on a 7.0 T small animal MRI system. We found that GBM showed a signal drop or negative (hypointense) enhancement on T_2-weighted MR images after intravenous injection of CLIO and CLIO-ICT, while PBS or ICT-administered mice showed little or no loss in tumor signal (Fig. 3c, 3d). When

comparing pre-and post-injection images in each group, we found that tumor T_2 relaxation times decreased significantly after CLIO and CLIO-ICT injection ($p < 0.005$) and did not change significantly after ICT or PBS injection (Fig. 3c, 3d). When comparing different treatment groups, tumor T_2 relaxation times of CLIO and CLIO-ICT-treated tumors were significantly shorter compared to the ICT only and PBS groups ($p < 0.05$). This was consistent with histopathological evaluations: Prussian blue staining demonstrated iron deposits within CLIO and CLIO-ICT-treated groups, but not PBS or ICT-treated groups (Fig. 3a).

Next, longitudinal MR scans were obtained on week 1 and 2 for each group to non-invasively monitor therapy response in tumors. For each time point, tumor volume was calculated and plotted against time. CLIO-ICT was most effective in inhibiting tumor growth (Fig. 3e). In addition, the degree of tumor T_2 signal enhancement, quantified as tumor T_2 relaxation time, correlated with tumor volume (Spearman rank correlation, $r=0.7$; $p<0.001$). Thus, CLIO-ICTs could be used for noninvasive monitoring of drug delivery and therapy response in orthotopic GBM models using MRI.

To understand the therapeutic mechanism, we evaluated the effect of CLIO-ICT on tumor vasculature and GICs. We used CD31 as a marker for GBM endothelial cells (7,40). Both CLIO-ICT and ICT treatment significantly inhibited microvessel density in pcGBM39 tumors ($p < 0.05$; Fig. 4). In addition, CLIO-ICT significantly reduced the GICs in pcGBM39–bearing mice, as demonstrated by reduced staining for CD133, CD15 and Nestin ($p < 0.005$; Fig. 4,) and significantly increased staining for Annexin-V/Dapi ($p <$

0.05; Fig. 5). We confirmed this observation using flow cytometry and firefly-luciferase-GFP expressing pcGBM2 cells. We observed that CLIO-ICTs triggers GBM cell apoptosis *in vivo*, as GBM cells (GFP-positive) from CLIO-ICT-treated mice presented higher levels of Annexin-V and DAPI staining compared to glioblastoma cells from vehicle-treated mice (Fig. 5a, 5b). Of note, CLIO-ICT did not induce apoptosis in non-tumor stromal (GFP-negative) cells (Fig. 5b, 5c), further confirming the absence of toxicity of this drug on normal cells. The percentage of $CD15^+$ GICs was significantly reduced in presence of CLIO-ICTs whereas apoptosis staining in $CD15^+$ GICs from CLIO-ICT-treated mice was significantly increased ($p < 0.05$; Fig. 5b, 5d).

The above results suggest that the therapeutic efficacy of CLIO-ICT is due to disruption of tumor vasculature and GIC apoptosis.

CLIO-ICTs in combination with temozolomide impedes tumor growth and improves survival in GBM-bearing animals.

Next, we assessed whether CLIO-ICT could be used in combination with standard clinical anti-GBM treatment, such as temozolomide (TMZ). Before proceeding to *in vivo* studies, a panel of GBM cells was screened *in vitro* for TMZ sensitivity with MTS-based viability assays, which demonstrated varying profiles of TMZ toxicity (Fig. 6a). For our *in vivo* studies, we proceeded with TMZ responsive pcGBM39 and pcGBM2 cells to test if CLIO-ICT would add therapeutic benefit. At three and eight weeks post-intracranial injection, pcGBM39 and pcGBM2-bearing mice were randomized into treatment groups: TMZ (200 mg/kg; cumulative dose) was orally administered either alone or in

combination with ICT/CLIO-ICT (80mg/kg; cumulative dose), twice per week for three consecutive weeks. At 3 weeks after initiation of treatment, MRI scans revealed 7 fold reduction in tumor size for TMZ plus CLIO-ICT-treated pcGBM39-bearing mice relative to that of vehicle-treated mice, which showed 30 fold increase in tumor size after treatment (Fig. 6b, 6c). The combination of TMZ plus CLIO-ICT significantly inhibited pcGBM39 tumor growth ($p < 0.005$), induced complete remission of pcGBM2 tumors and increased overall survival as compared to TMZ plus ICT and single drug regimens (Fig. 6d-i).

Discussion

Data showed that novel MMP-14-activatable cross-linked iron oxide nanoparticles (CLIO-ICT), which where conjugated with the VDA ICT (a structural analogue of ICT2588), caused significant apoptosis of cancer cells and GIC in GBM. This led to significantly prolonged survival of pcGBM39 bearing mice and complete tumor remission of pcGBM2 bearing mice. CLIO-ICT synergized with temozolomide *in vivo*, thereby revealing a novel therapeutic combinatorial regimen for targeting GBMs.

Current GBM therapies include surgical resection followed by radiation therapy with concurrent temozolomide (TMZ) treatment (41). However 90% of GBM patients develop tumor recurrence (42). This is partly attributed to poor drug delivery and drug resistant GIC (43). Nearly all large molecules and the majority of small molecular drugs including tyrosine kinase inhibitors are effluxed at the blood brain barrier by P-gp and Bcrp on the luminal side of endothelial cells, and never reach therapeutic levels in the brain (44). Another major challenge involves the multiple molecular pathways of GBMs.

Identifying just one therapeutic target is insufficient, as this does not account for the considerable array of genetic and epigenetic heterogeneities found within and among GBM patients (45). Our approach addresses most of these challenges: CLIO-ICT does not rely solely on a passive delivery across the tumor microvessel wall via the EPR effect (9,10). The VDA rather increases vascular permeability through active disruption of the tumor microvessel endothelial lining. This effect is specific to tumor vessels through tumor enzyme activation (28), and efficacious in tumors with different molecular codes. Both ICT-mediated vessel disruption and nanoparticle-mediated enhanced permeability and retention (EPR) support accumulation of CLIO-ICT in the tumor interstitium. CLIO-ICT causes tumor blood vessel collapse, cancer cell starvation and jeopardizes the tumor microenvironment, making this a very effective therapeutic strategy (26). We further demonstrate for the first time that CLIO-ICT is capable of inducing apoptosis in GBM initiating cells (GICs).

Agemy *et al.* reported that theranostic nanoparticles linked to a tumor vasculature homing peptide (CGKRK) showed exceptional efficacy in eliminating a lentivirus-induced GBM model. However, this drug could not completely inhibit the growth of orthotopically transplanted GBM (46). By contrast, our CLIO-ICT achieved almost complete remission of orthotopic pcGBM2 tumors and significantly inhibited pcGBM39 tumors, both of which express MMP-14. Literature shows that MMP-14 expression is positively correlated with tumor grade and disease progression of gliomas (23,47). Therefore our MMP-14 targeted approach seems specifically suited for the treatment of high grade GBMs.

Since our theranostic nanoparticles are based on two clinically applicable components, the combined CLIO-ICT has high potential for clinical translation: CLIO-ICT is composed of the FDA-approved nanoparticle compound ferumoxytol, linked to a VDA based on ICT2588. ICT2588 is on course to be evaluated in a phase I clinical trial in the UK for treatment of advanced tumors outside of the CNS in 2017. Further since CLIO-ICT are activated by tumor MMP-14 to release the potent VDA specifically in tumor tissue, potential side effects of cardiotoxicity, as noted with previous VDAs, are minimized (28).

VDA-based strategies sensitize GBMs to chemotherapy through three mechanisms: (1) VDAs jeopardize the perivascular GIC niche, which provides access to vascular nutritions but shields GIC from classical chemotherapy agents, such as TMZ. (2) VDAs disrupt tumor-promoting vascular endothelial cells. Borovski *et al.,* found that tumor microvascular endothelial cells (tMVECs) isolated from human GBM tumors promoted the proliferation of human CD133+ cells when GIC-tMVEC co-cultures were exposed to irradiation and TMZ (48,49). By contrast, CLIO-ICT had inhibited both tumor endothelial cells and GIC, thereby eliminating endothelial cell-mediated GIC rescue. (3) CLIO-ICT is activated by tumor-specific enzymes, i.e. the activation is “built-in” and does not rely on external stimuli. By contrast, previous generations of theranostic nanoparticles had to be activated by near-infrared phototherapy (50). These approaches are more difficult to translate to the clinic and were accompanied with severe side effects, such as severe cerebral edema (50).

In summary CLIO-ICT holds significant clinical potential for improving targeted therapy and survival in GBM patients. Significant advantages of CLIO-ICT compared to other theranostic agents include selective and effective delivery to GBM, therapeutic efficacy independent of EPR effect, prolonged retention in the tumor tissue via VDA initiated vascular collapse, drug entrapment in the GIC niche, ability to track the drug with MRI and eliminated toxicity-liability to normal organs. Further our approach of combining CLIO-ICT with TMZ offers refinements to current less optimal standards of care in order to achieve GBM remission.

Acknowledgements

We thank the Small Animal Imaging Facility at Stanford for providing the equipment and infrastructure for this project. We thank Jamal Elbakay for technical assistance. We thank members of the Daldrup-Link, Gambhir, and Cheshier and ICT Bradford laboratories for valuable discussions. This work was in part supported by grants from the National Cancer Institute: Grants R21CA176519 and R21CA190196 to HEDL and a CCNE-TD U54 grant (1U54CA199075) to SSG. JK's contribution to this work was supported in part by an NCI training grant: T32 CA118681. A University of Bradford Commercial Development Fund award (to RAF) provided support towards the costs associated with chemical synthesis.

References

1. Sturm D, Bender S, Jones DT, Lichter P, Grill J, Becher O, et al. Paediatric and adult glioblastoma: multiform (epi)genomic culprits emerge. Nat Rev Cancer 2014;14(2):92-107.
2. Stupp R, Mason WP, van den Bent MJ, Weller M, Fisher B, Taphoorn MJ, et al. Radiotherapy plus concomitant and adjuvant temozolomide for glioblastoma. N Engl J Med 2005;352(10):987-96.
3. Schonberg DL, Lubelski D, Miller TE, Rich JN. Brain tumor stem cells: Molecular characteristics and their impact on therapy. Mol Aspects Med 2014;39:82-101.
4. Folkins C, Shaked Y, Man S, Tang T, Lee CR, Zhu Z, et al. Glioma tumor stem-like cells promote tumor angiogenesis and vasculogenesis via vascular endothelial growth factor and stromal-derived factor 1. Cancer Res 2009;69(18):7243-51.
5. Beier D, Schulz JB, Beier CP. Chemoresistance of glioblastoma cancer stem cells--much more complex than expected. Mol Cancer 2011;10:128.
6. Calabrese C, Poppleton H, Kocak M, Hogg TL, Fuller C, Hamner B, et al. A perivascular niche for brain tumor stem cells. Cancer Cell 2007;11(1):69-82.
7. Cheng L, Huang Z, Zhou W, Wu Q, Donnola S, Liu JK, et al. Glioblastoma stem cells generate vascular pericytes to support vessel function and tumor growth. Cell 2013;153(1):139-52.
8. Gilbertson RJ, Rich JN. Making a tumour's bed: glioblastoma stem cells and the vascular niche. Nat Rev Cancer 2007;7(10):733-6.
9. Mura S, Couvreur P. Nanotheranostics for personalized medicine. Adv Drug Deliv Rev 2012;64(13):1394-416.
10. Jain RK, Stylianopoulos T. Delivering nanomedicine to solid tumors. Nat Rev Clin Oncol 2010;7(11):653-64.
11. Davis PD, Dougherty GJ, Blakey DC, Galbraith SM, Tozer GM, Holder AL, et al. ZD6126: a novel vascular-targeting agent that causes selective destruction of tumor vasculature. Cancer Res 2002;62(24):7247-53.
12. Kanthou C, Tozer GM. Microtubule depolymerizing vascular disrupting agents: novel therapeutic agents for oncology and other pathologies. Int J Exp Pathol 2009;90(3):284-94.
13. Tozer GM, Kanthou C, Baguley BC. Disrupting tumour blood vessels. Nat Rev Cancer 2005;5(6):423-35.
14. Ley CD, Horsman MR, Kristjansen PE. Early effects of combretastatin-A4 disodium phosphate on tumor perfusion and interstitial fluid pressure. Neoplasia 2007;9(2):108-12.
15. Reyes-Aldasoro CC, Wilson I, Prise VE, Barber PR, Ameer-Beg M, Vojnovic B, et al. Estimation of apparent tumor vascular permeability from multiphoton fluorescence microscopic images of P22 rat sarcomas in vivo. Microcirculation 2008;15(1):65-79.
16. Seshadri M, Ciesielski MJ. MRI-based characterization of vascular disruption by 5,6-dimethylxanthenone-acetic acid in gliomas. J Cereb Blood Flow Metab 2009;29(8):1373-82.
17. Grossmann KF, Colman H, Akerley WA, Glantz M, Matsuoko Y, Beelen AP, et al. Phase I trial of verubulin (MPC-6827) plus carboplatin in patients with relapsed glioblastoma multiforme. J Neurooncol 2012;110(2):257-64.
18. Hinnen P, Eskens FA. Vascular disrupting agents in clinical development. Br J Cancer 2007;96(8):1159-65.

19. van Heeckeren WJ, Bhakta S, Ortiz J, Duerk J, Cooney MM, Dowlati A, et al. Promise of new vascular-disrupting agents balanced with cardiac toxicity: is it time for oncologists to get to know their cardiologists? J Clin Oncol 2006;24(10):1485-8.
20. Cooney MM, Radivoyevitch T, Dowlati A, Overmoyer B, Levitan N, Robertson K, et al. Cardiovascular safety profile of combretastatin a4 phosphate in a single-dose phase I study in patients with advanced cancer. Clin Cancer Res 2004;10(1 Pt 1):96-100.
21. Atkinson JM, Siller CS, Gill JH. Tumour endoproteases: the cutting edge of cancer drug delivery? Br J Pharmacol 2008;153(7):1344-52.
22. Ulasov I, Yi R, Guo D, Sarvaiya P, Cobbs C. The emerging role of MMP14 in brain tumorigenesis and future therapeutics. Biochim Biophys Acta 2014;1846(1):113-20.
23. Markovic DS, Vinnakota K, Chirasani S, Synowitz M, Raguet H, Stock K, et al. Gliomas induce and exploit microglial MT1-MMP expression for tumor expansion. Proc Natl Acad Sci U S A 2009;106(30):12530-5.
24. Hambardzumyan D, Gutmann DH, Kettenmann H. The role of microglia and macrophages in glioma maintenance and progression. Nat Neurosci 2016;19(1):20-7.
25. Coussens LM, Fingleton B, Matrisian LM. Cancer therapy - Matrix metalloproteinase inhibitors and cancer: Trials and tribulations. Science 2002;295(5564):2387-92.
26. Atkinson JM, Falconer RA, Edwards DR, Pennington CJ, Siller CS, Shnyder SD, et al. Development of a novel tumor-targeted vascular disrupting agent activated by membrane-type matrix metalloproteinases. Cancer Res 2010;70(17):6902-12.
27. Ueda J, Kajita M, Suenaga N, Fujii K, Seiki M. Sequence-specific silencing of MT1-MMP expression suppresses tumor cell migration and invasion: importance of MT1-MMP as a therapeutic target for invasive tumors. Oncogene 2003;22(54):8716-22.
28. Gill JH, Loadman PM, Shnyder SD, Cooper P, Atkinson JM, Ribeiro Morais G, et al. Tumor-targeted prodrug ICT2588 demonstrates therapeutic activity against solid tumors and reduced potential for cardiovascular toxicity. Mol Pharm 2014;11(4):1294-300.
29. Ansari C, Tikhomirov GA, Hong SH, Falconer RA, Loadman PM, Gill JH, et al. Development of novel tumor-targeted theranostic nanoparticles activated by membrane-type matrix metalloproteinases for combined cancer magnetic resonance imaging and therapy. Small 2014;10(3):566-75, 417.
30. Chang E, Pohling C, Natarajan A, Witney TH, Kaur J, Xu L, et al. AshwaMAX and Withaferin A inhibits gliomas in cellular and murine orthotopic models. J Neurooncol 2016;126(2):253-64.
31. Weidner N, Semple JP, Welch WR, Folkman J. Tumor angiogenesis and metastasis--correlation in invasive breast carcinoma. N Engl J Med 1991;324(1):1-8.
32. Fenton TR, Nathanson D, Ponte de Albuquerque C, Kuga D, Iwanami A, Dang J, et al. Resistance to EGF receptor inhibitors in glioblastoma mediated by phosphorylation of the PTEN tumor suppressor at tyrosine 240. Proc Natl Acad Sci U S A 2012;109(35):14164-9.
33. Aghighi M, Golovko D, Ansari C, Marina NM, Pisani L, Kurlander L, et al. Imaging Tumor Necrosis with Ferumoxytol. PLoS One 2015;10(11):e0142665.
34. Iv M, Telischak N, Feng D, Holdsworth SJ, Yeom KW, Daldrup-Link HE. Clinical applications of iron oxide nanoparticles for magnetic resonance imaging of brain tumors. Nanomedicine (Lond) 2015;10(6):993-1018.

35. Daldrup-Link HE, Mohanty S, Ansari C, Lenkov O, Shaw A, Ito K, et al. Alk5 inhibition increases delivery of macromolecular and protein-bound contrast agents to tumors. JCI Insight 2016;1(6).
36. Daldrup-Link HE, Rummeny EJ, Ihssen B, Kienast J, Link TM. Iron-oxide-enhanced MR imaging of bone marrow in patients with non-Hodgkin's lymphoma: differentiation between tumor infiltration and hypercellular bone marrow. Eur Radiol 2002;12(6):1557-66.
37. Zanganeh S, Hutter G, Spitler R, Lenkov O, Mahmoudi M, Shaw A, et al. Iron oxide nanoparticles inhibit tumour growth by inducing pro-inflammatory macrophage polarization in tumour tissues. Nat Nanotechnol 2016.
38. Patru C, Romao L, Varlet P, Coulombel L, Raponi E, Cadusseau J, et al. CD133, CD15/SSEA-1, CD34 or side populations do not resume tumor-initiating properties of long-term cultured cancer stem cells from human malignant glio-neuronal tumors. BMC Cancer 2010;10:66.
39. Assad Kahn S, Costa SL, Gholamin S, Nitta RT, Dubois LG, Feve M, et al. The anti-hypertensive drug prazosin inhibits glioblastoma growth via the PKCdelta-dependent inhibition of the AKT pathway. EMBO Mol Med 2016;8(5):511-26.
40. Ricci-Vitiani L, Pallini R, Biffoni M, Todaro M, Invernici G, Cenci T, et al. Tumour vascularization via endothelial differentiation of glioblastoma stem-like cells. Nature 2010;468(7325):824-8.
41. Nguyen LT, Touch S, Nehme-Schuster H, Antoni D, Eav S, Clavier JB, et al. Outcomes in newly diagnosed elderly glioblastoma patients after concomitant temozolomide administration and hypofractionated radiotherapy. Cancers (Basel) 2013;5(3):1177-98.
42. Ramirez YP, Weatherbee JL, Wheelhouse RT, Ross AH. Glioblastoma multiforme therapy and mechanisms of resistance. Pharmaceuticals (Basel) 2013;6(12):1475-506.
43. Chen J, Li Y, Yu TS, McKay RM, Burns DK, Kernie SG, et al. A restricted cell population propagates glioblastoma growth after chemotherapy. Nature 2012;488(7412):522-6.
44. Singh SK, Hawkins C, Clarke ID, Squire JA, Bayani J, Hide T, et al. Identification of human brain tumour initiating cells. Nature 2004;432(7015):396-401.
45. Prados MD, Byron SA, Tran NL, Phillips JJ, Molinaro AM, Ligon KL, et al. Toward precision medicine in glioblastoma: the promise and the challenges. Neuro Oncol 2015;17(8):1051-63.
46. Agemy L, Friedmann-Morvinski D, Kotamraju VR, Roth L, Sugahara KN, Girard OM, et al. Targeted nanoparticle enhanced proapoptotic peptide as potential therapy for glioblastoma. Proc Natl Acad Sci U S A 2011;108(42):17450-5.
47. Nuttall RK, Pennington CJ, Taplin J, Wheal A, Yong VW, Forsyth PA, et al. Elevated membrane-type matrix metalloproteinases in gliomas revealed by profiling proteases and inhibitors in human cancer cells. Mol Cancer Res 2003;1(5):333-45.
48. Borovski T, Beke P, van Tellingen O, Rodermond HM, Verhoeff JJ, Lascano V, et al. Therapy-resistant tumor microvascular endothelial cells contribute to treatment failure in glioblastoma multiforme. Oncogene 2013;32(12):1539-48.

49. Borovski T, Verhoeff JJ, ten Cate R, Cameron K, de Vries NA, van Tellingen O, et al. Tumor microvasculature supports proliferation and expansion of glioma-propagating cells. Int J Cancer 2009;125(5):1222-30.
50. Jing H, Weidensteiner C, Reichardt W, Gaedicke S, Zhu X, Grosu AL, et al. Imaging and Selective Elimination of Glioblastoma Stem Cells with Theranostic Near-Infrared-Labeled CD133-Specific Antibodies. Theranostics 2016;6(6):862-74.

Figures and Legends

Figure 1. CLIO-ICTs inhibit GBM and GIC survival *in vitro*. (a) Schematic demonstration of CLIO-ICT activation in presence of tumor enzyme MMP-14, to release the active drug, azademethylcolchicine. Azademethylcolchicine targets tubulin to induce apoptosis in tumor cells. **(b)** Representative T_2 weighted MR images of CLIO-ICT and ferumoxytol at different dilutions. T_2 MSME sequences were used to generate R_2 relaxivites. R_2 relaxivities of CLIO-ICT (blue line) and ferumoxytol (red line). **(c)** Graphical representation of MMP-14 expression in different GBM cells lines. MMP-14 expression was measured with q-PCR assay, GAPDH served as endogenous control. **(d)** Viability analysis of GBMs treated with CLIO-ICT (10nM), ICT (10nM), CLIO (0.01mM) and PBS. GBMs were treated for 96 hrs and viability was assayed using MTS assay. **(e)** Graph shows fold change for cleaved caspase-3 in control and treated GBM cells. Cleaved caspase-3 fluorescence signals were detected by SensoLyte Homogeneous AMC Caspase-3/7 assay kit and the fold change was represented by the ratio: fluorescence signals in treated/fluorescence signals in control. **(f)** Annexin-V/PI apoptosis staining in control and treated GBM39 cells (Left panel). Right panel depicts quantification for percentage apoptosis in A172, U87 and pcGBM39 cells after 48 hrs of

treatment. **(g)** Immunofluorescence for α-tubulin in control and treated U87 cells. Upper panel shows confocal images and lower panel depicts quantification of tubulin signals scale bar 10μm. **(h)** Flow cytometry analysis of GIC markers (CD133, CD15 and CD49F), Annexin V/DAPI staining in control and treated pcGBM39 cells. CLIO-ICT-treated pcGBM39 were subjected to flow cytometric staining for GIC surface markers (upper panel) and apoptosis markers (lower panel). **(i)** Graph shows percentages of $CD133^+$, $CD15^+$ and $CD49F^+$ GICs (left) and percentage apoptosis (right) in gated $CD133^+$, $CD15^+$ and $CD49F^+$ GICs from control and treated pcGBM39 cells. Results are represented as mean ± SD from three independent experiments. *$P < 0.05$, **$P < 0.005$, one-way ANOVA.

Figure 2. CLIO-ICTs retard GBM growth *in vivo*. (a) Schematic demonstration of CLIO-ICT-mediated anti-GBM effect. In presence of tumor enzyme MMP-14, CLIO-ICT is cleaved to release the active vasculature-disrupting agent, azademethylcolchicine. Activated CLIO-ICT targets tumor vasculature and induces apoptosis in GICs and GBMs, thereby inhibiting GBM growth and improving survival outcomes. **(b)** Schematic representation of experimental design. Tumors were initiated with orthotopic injections of primary human GBM samples (pcGBM39 cells and pcGBM2 cells that express luciferase and GFP-luciferase construct respectively) into the striatum of NSG mice. Treatment was initiated once the tumors were detected and bioluminescent analyses were performed during and after treatment. **(c)** Bioluminescent *in vivo* images of tumors in mice treated with CLIO-ICT (0.5 mmol Fe/kg and 80mg/kg of ICT), ICT (80mg/kg of ICT), CLIO (0.5 mmol Fe/kg) or vehicle. **(d)** Quantification of the bioluminescent signals.

Fold change in total flux represents the ratio: total flux after treatment/total flux before treatment. *P = 0.0002 and *P = 0.0003 for pcGBM39 (n=8) and pcGBM2 (n=6), respectively, one-way ANOVA. **(e)** Kaplan–Meyer survival curves of control and treated mice demonstrate a significant survival benefit of CLIO-ICT as compared to vehicle, log-rank Mantel–Cox test.

Figure 3. CLIO-ICTs are delivered to GBM tumors and induce tumor apoptosis. Tumors were initiated with orthotopic injections of pcGBM39 tumors and mice were treated with CLIO-ICT (0.5 mmol Fe/kg and 80mg/kg of ICT), ICT (80mg/kg of ICT), CLIO (0.5 mmol Fe/kg) or vehicle. **(a)** Upper panel: Representative H&E staining for brain coronal sections from control and treated animals. White arrows indicate tumor. Objective 4X. Scale bar represents 100 μm. Middle panel: Prussian blue iron staining for control and treated tumors. Objective 4X. Scale bar represent 100μm. Lower panel: Prussian blue at higher magnification 10x for boxed regions in middle panel. Scale bar represent 40 μm **(b)** Representative immunofluorescence confocal images for cleaved caspase-3 in control and treated pcGBM39 tumors**.** Arrows indicate cleaved caspase-3 positive cells. Nuclei counterstained with DAPI. Scale bar represents 75 μm**.** Graph shows quantification for FITC and cleaved caspase-3 staining in control and treated pcGBM39 tumors. Results are represented as mean ± SD from three independent experiments. *P < 0.05, **P < 0.005, one-way ANOVA. **(c)** Representative T_2 weighted MR images of mice brain. T_2 FSE sequences were used to capture coronal T_2 weighted images. Nanoparticle and theranostic nanoparticle delivery is demonstrated by T_2 darkening or negative enhancement in CLIO and CLIO-ICT treated animals

respectively. On day 14 tumor periphery is marked by dotted yellow line. **(d)** Quantification of T_2 darkening. T_2 MSME sequences were used to generate T_2 maps, Osirix software was used to calculate T_2 values. CLIO and CLIO-ICT-treated tumors demonstrated shorter T_2 values corresponding to T_2 darkening or negative enhancement. **(e)** Quantification of tumor volumes before and after treatment. T_2 weighted MR scans were used to calculate tumor volumes using Osirix software. *P < 0.05, **P < 0.005, n=6, one-way ANOVA.

Figure 4. CLIO-ICTs target GBM vasculature and GICs *in vivo*. Tumors were established with orthotopic injections of pcGBM39 cells. Mice were treated with CLIO-ICT (0.5 mmol Fe/kg and 80mg/kg of ICT), ICT (80mg/kg of ICT), CLIO (0.5 mmol Fe/kg) or vehicle. Representative immunofluorescent confocal images depicting CD31, CD133, CD15 and Nestin staining in pcGBM39 tumors. CD31 is used to outline tumor vasculature. CD133, CD15 and nestin are used to mark GICs. Signal intensity for CD31, CD133, CD15 and nestin in control and treated tumors have been quantified and represented graphically. Scale bar represent 20 μm (CD31) and 10 μm (CD133, CD15 and nestin). Results are representative of three independent experiments. *P < 0.05, **P < 0.005, one-way ANOVA.

Figure 5. CLIO-ICTs induce GIC apoptosis *in vivo.* Tumors were initiated with orthotopic injections of pcGBM2 cells. Mice were treated with CLIO-ICT (0.5 mmol Fe/kg and 80mg/kg of ICT), ICT (80mg/kg of ICT), CLIO (0.5 mmol Fe/kg) or vehicle. Flow cytometric analysis of GIC markers (CD15), Annexin V and DAPI in **(a)** vehicle and

(b) CLIO-ICT-treated pcGBM2 tumors. GFP positive pcGBM2 tumors were gated and analyzed for percentage apoptosis in both **(c)** pcGBM2 cells and **(d)** GICs from pcGBM2. $P < 0.05$, $^{**}P < 0.005$, n=6, one-way ANOVA.

Figure 6. CLIO-ICTs increase the anti-tumor efficacy of temozolomide (TMZ) *in vivo*. (a) *In vitro* analysis of TMZ chemosensitivity by cell viability assay. Panel of GBM cells were exposed to increasing doses of TMZ (0-500 μM) for 72hrs and cell viability was calculated by MTS assay. For *in vivo* experiments**,** tumors were initiated with orthotopic injections of pcGBM39 cells (b-f) and pcGBM2 cells (g-i). Mice were treated with TMZ alone (200mg/kg) or in combination with CLIO-ICT (0.5 mmol Fe/kg and 80mg/kg of ICT) and ICT (80mg/kg of ICT), CLIO (0.5 mmol Fe/kg) or vehicle. **(b)** Representative T_2 weighted MR images of mice brain. T_2 FSE sequences were used to capture coronal T_2 weighted images. Yellow dotted line represents tumor periphery. **(c)** Quantification of tumor volumes before and after treatment. T_2 weighted MR scans were used to calculate tumor volumes using Osirix software. Bioluminescent *in vivo* images of tumors in control and treated mice in pcGBM39 **(d)** and pcGBM2 **(g)** tumor models. **(e and h)** Quantification of the bioluminescent signals. Fold change in total flux represents the ratio: total flux after treatment/total flux before treatment. $^{*}P <$ 0.05, respectively, n = 6 (pcGBM39) and n = 6 (pcGBM2), one-way ANOVA. **(f and i)** Kaplan–Meyer survival curves of control and treated mice (n=6, pcGBM39; n=6, pcGBM2) demonstrate a significant survival benefit of CLIO-ICT and ICT in combination with TMZ as compared to vehicle, log-rank Mantel–Cox test. $^{*}P < 0.05$, $^{**}P < 0.005$, n=6, one-way ANOVA.

Author Manuscript Published OnlineFirst on June 28, 2017; DOI: 10.1158/1535-7163.MCT-17-0022
Author manuscripts have been peer reviewed and accepted for publication but have not yet been edited.

Figure1

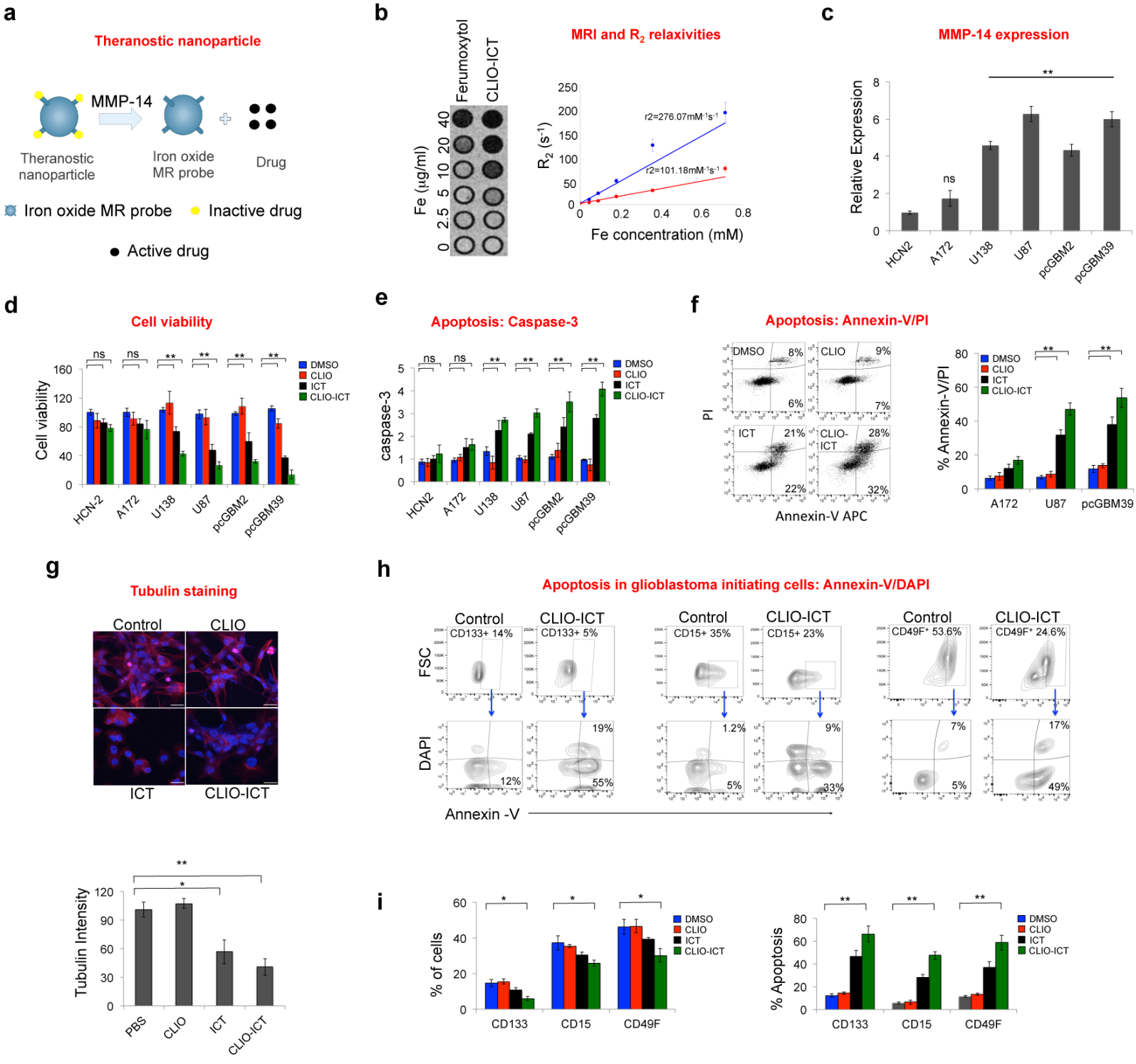

Author Manuscript Published OnlineFirst on June 28, 2017; DOI: 10.1158/1535-7163.MCT-17-0022
Author manuscripts have been peer reviewed and accepted for publication but have not yet been edited.

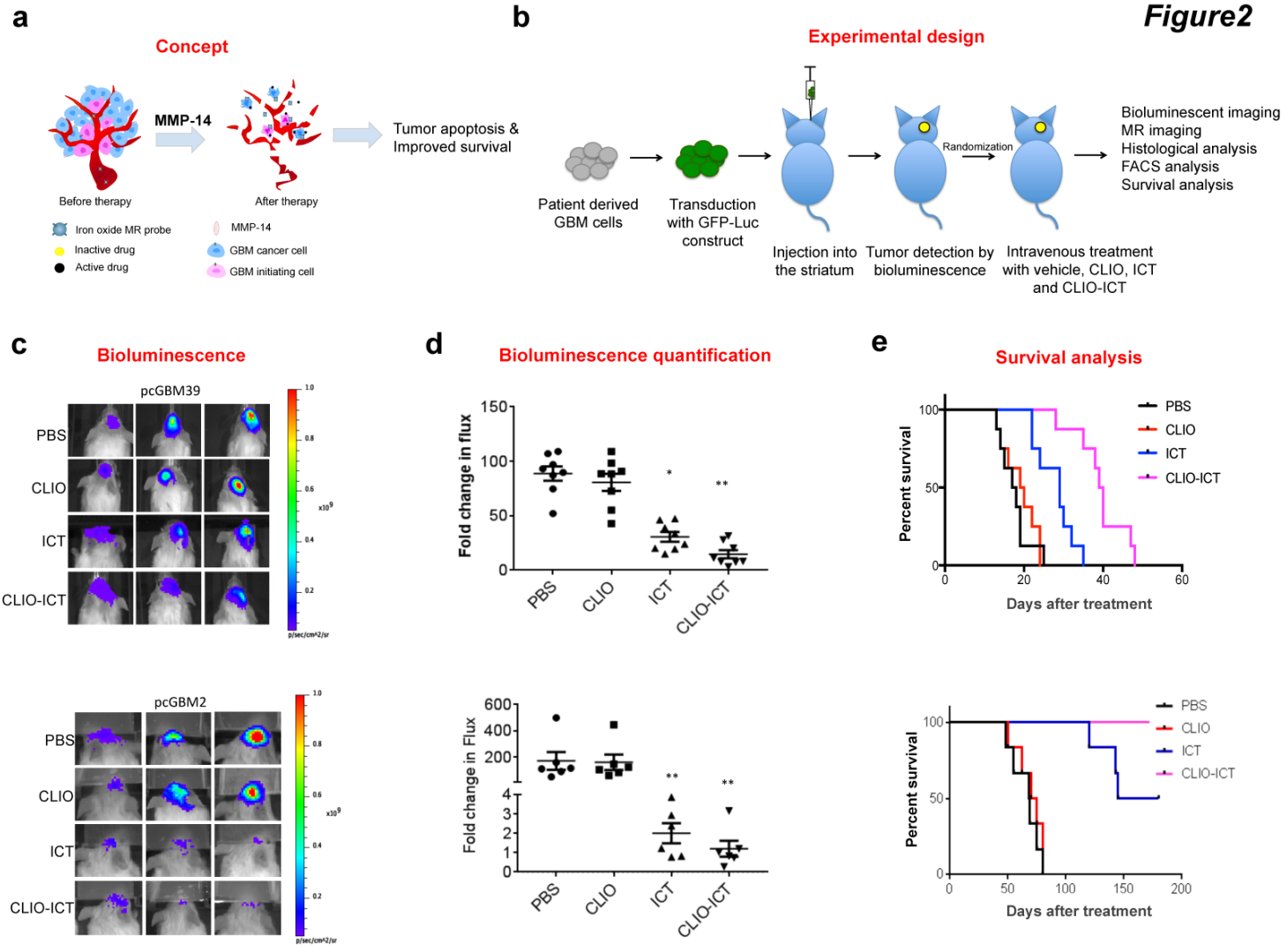

Figure2

Author Manuscript Published OnlineFirst on June 28, 2017; DOI: 10.1158/1535-7163.MCT-17-0022
Author manuscripts have been peer reviewed and accepted for publication but have not yet been edited.

Figure 3

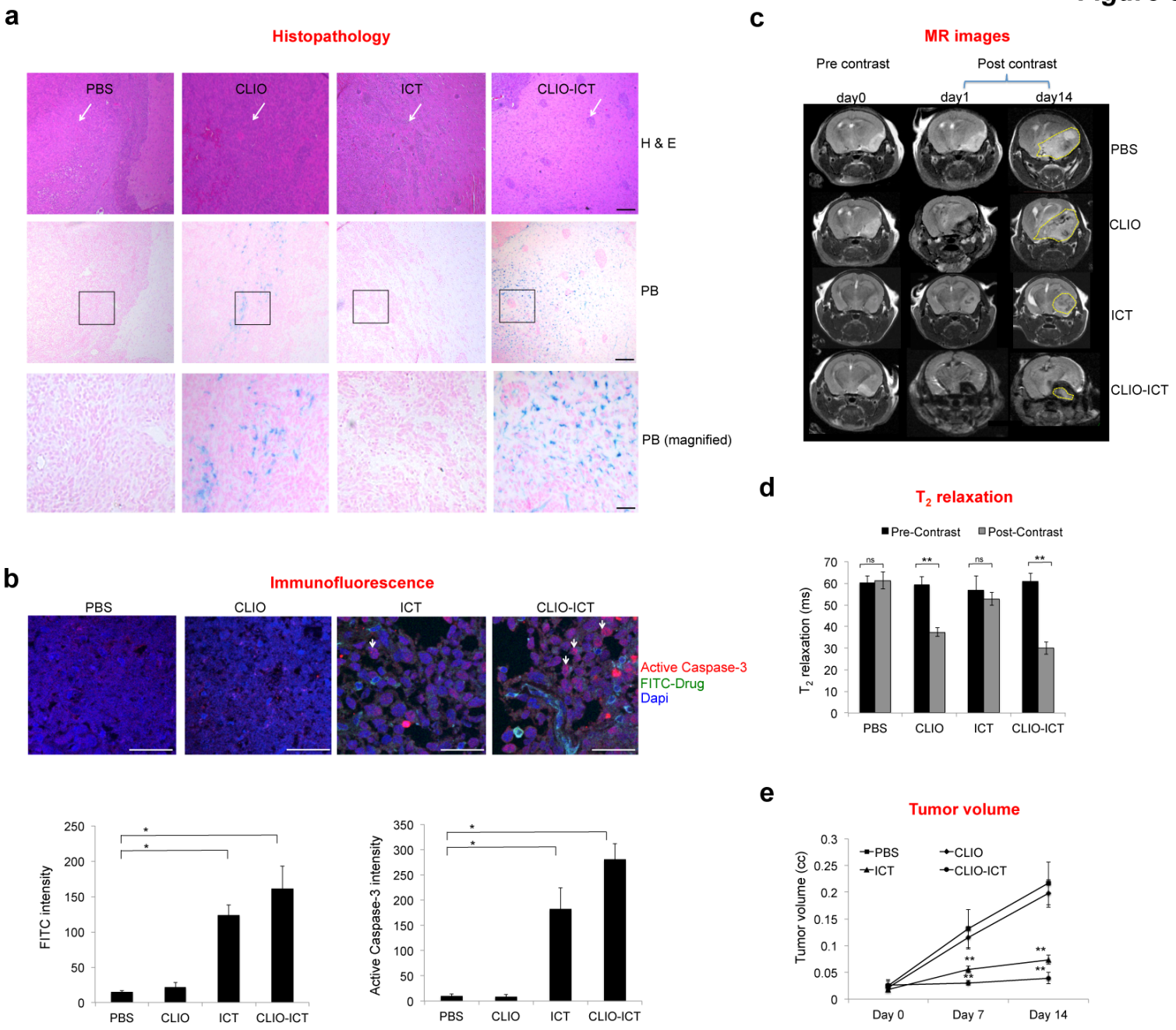

Author Manuscript Published OnlineFirst on June 28, 2017; DOI: 10.1158/1535-7163.MCT-17-0022
Author manuscripts have been peer reviewed and accepted for publication but have not yet been edited.

Figure 4

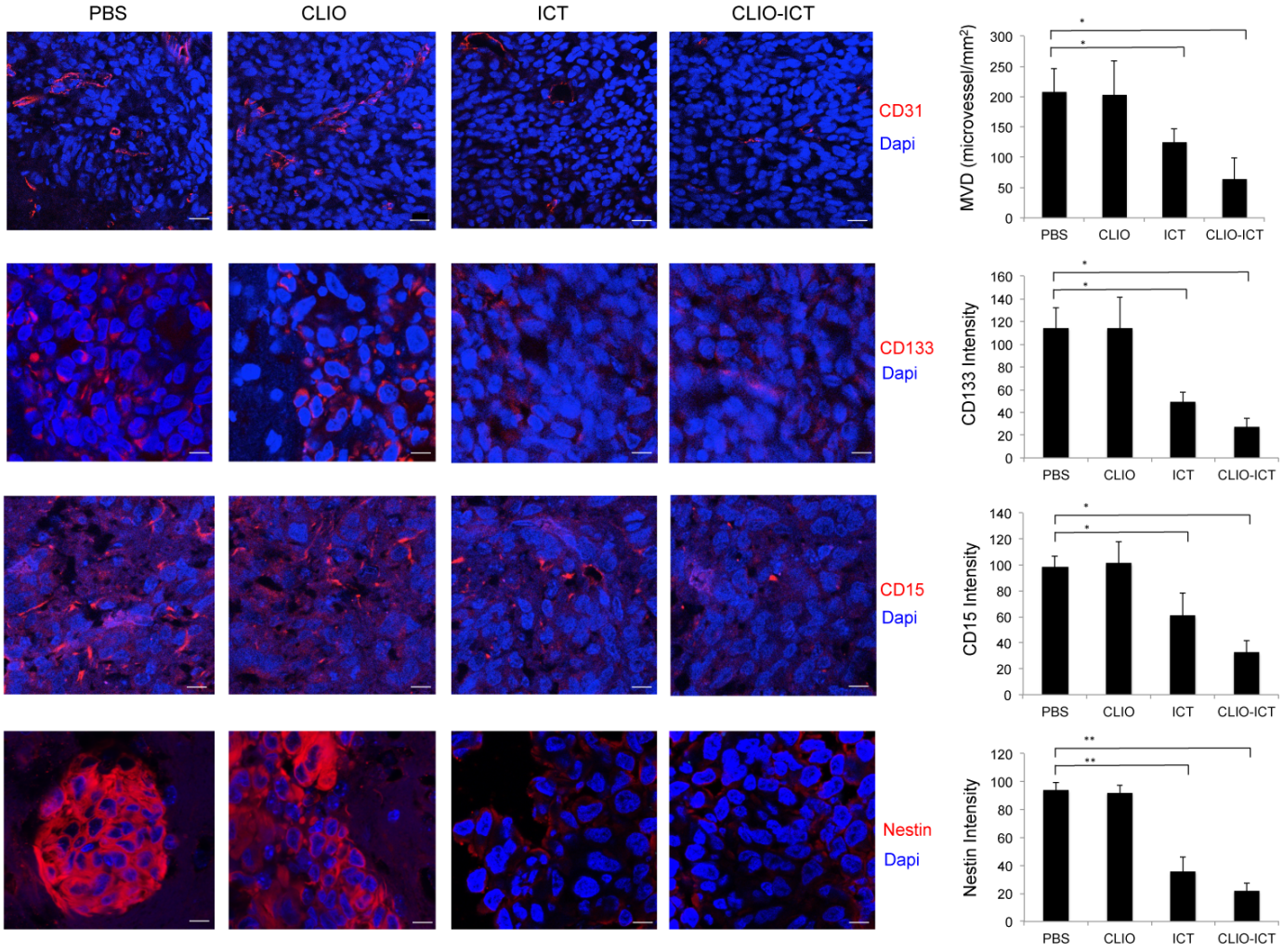

Author Manuscript Published OnlineFirst on June 28, 2017; DOI: 10.1158/1535-7163.MCT-17-0022
Author manuscripts have been peer reviewed and accepted for publication but have not yet been edited.

Figure 5

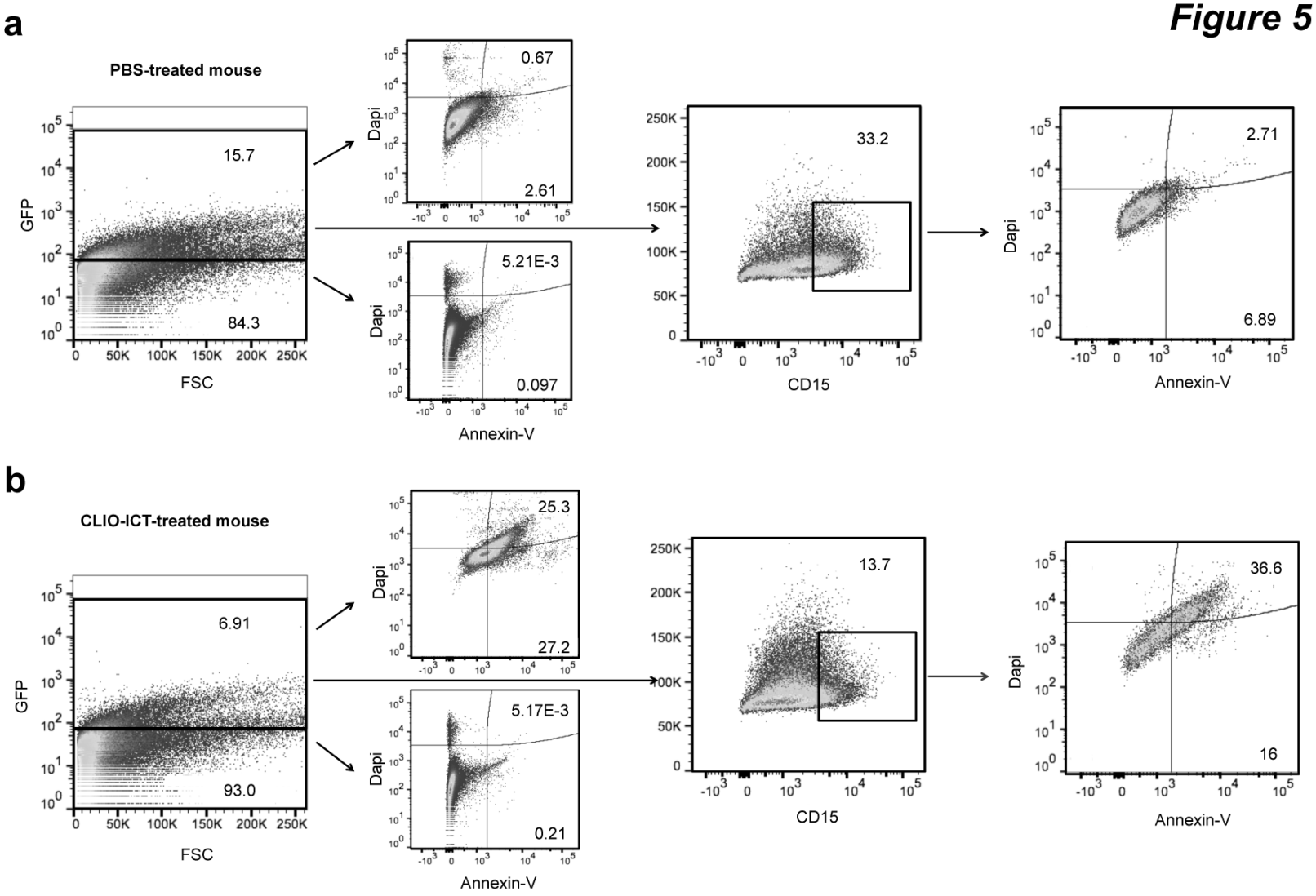

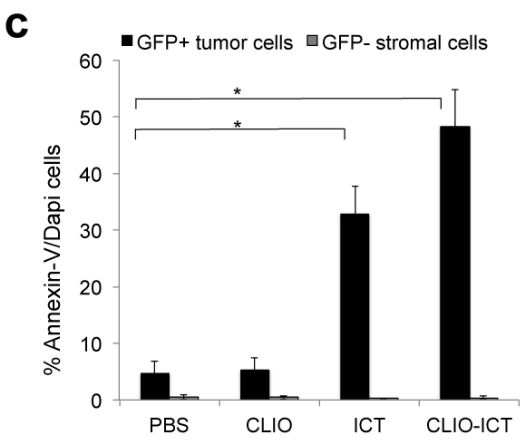

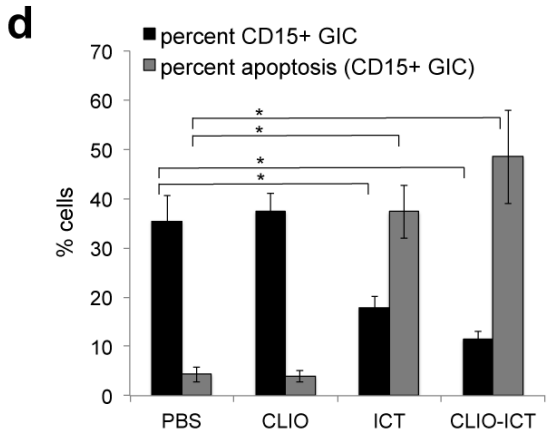

Author Manuscript Published OnlineFirst on June 28, 2017; DOI: 10.1158/1535-7163.MCT-17-0022
Author manuscripts have been peer reviewed and accepted for publication but have not yet been edited.

Figure 6

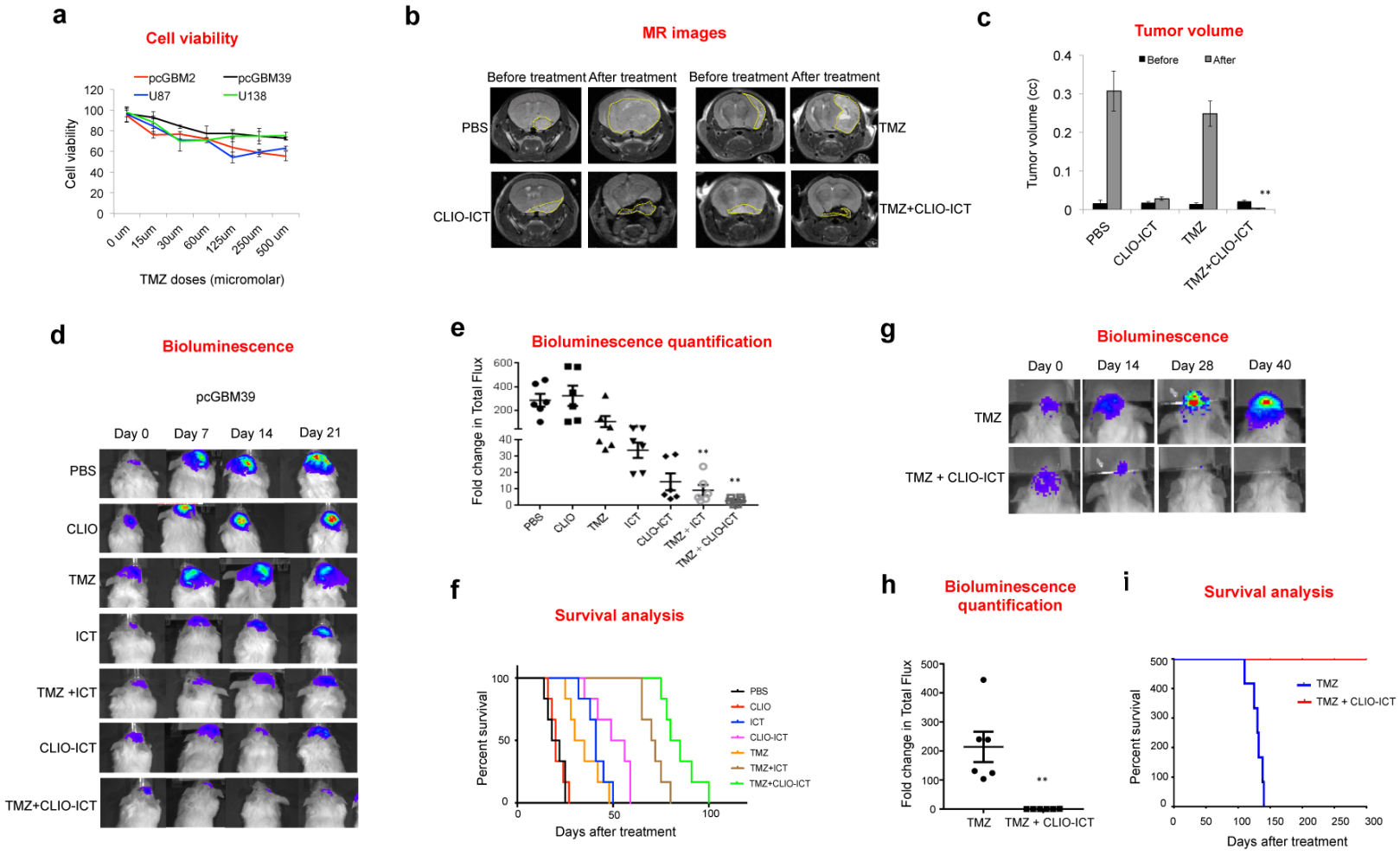

AACR American Association for Cancer Research

Molecular Cancer Therapeutics

A novel theranostic strategy for MMP-14 expressing glioblastomas impacts survival

Suchismita Mohanty, Zixin Chen, Kai Li, et al.

Mol Cancer Ther Published OnlineFirst June 28, 2017.